

Atomic Layer Deposition of MoS₂ Decorated TiO₂ Nanotubes for Photoelectrochemical Water Splitting

Chengxu Shen, Ewa Wierzbicka,* Thorsten Schultz, Rongbin Wang, Norbert Koch, and Nicola Pinna*

A thermal atomic layer deposition (ALD) process to fabricate MoS₂ thin films is successfully demonstrated by using cycloheptatriene molybdenum tricarbonyl (C₇H₈Mo(CO)₃) and H₂S as precursors at an ALD temperature below 300 °C. The process is systematically investigated, showing a typical self-limiting characteristic within an ALD temperature window of 225–285 °C and a high growth-per-cycle of 0.11 nm. The as-deposited films are amorphous while they can be crystallized in situ by sulfurization with H₂S at a low temperature of 300 °C. A prototypical application of the developed ALD process is demonstrated by constructing a MoS₂/TiO₂ heterostructure through depositing MoS₂ onto anodized TiO₂ nanotubes for photoelectrochemical water splitting. The MoS₂/TiO₂ heterostructures exhibit approximately three times superior photoelectrochemical performance than the pristine TiO₂ nanotubes. This is attributed to an enhanced visible light-harvesting ability of MoS₂ and an improved separation of the photo-generated charge carriers at the heterostructure interface, which is affirmed by a staggering gap (type II) between MoS₂ and TiO₂ as probed by ultraviolet photoelectron spectroscopy.

MoS₂/CdS,^[15] have demonstrated a high PEC performance. It was proven that the formation of such heterostructures is beneficial for the separation of photo-generated excitons (hole–electron pairs).^[13,14,16,17] In particular, MoS₂/TiO₂ heterostructures have attracted significant interest, as MoS₂ can be used as a photosensitizer for chemically stable but wide-bandgap TiO₂ semiconductor.^[18] The respective bandgap edge positions of the two semiconductors form a charge-transfer cascade, which significantly increases the separation of the photogenerated charge carriers.^[19,20] Overall, both the photosensitizing properties of MoS₂ and the electronic structure of the heterojunction create a suitable platform for UV and visible light utilization resulting in high PEC performance.


It should be noticed that the electronic and catalytic properties of MoS₂ are highly dependent on the film thickness and morphology,^[21] as well as the architecture of the substrates.^[22,23]

Therefore, various nanostructured architectures of TiO₂ (e.g., TiO₂ nanorods and nanotubes) have been applied as a scaffold to construct MoS₂/TiO₂ heterostructures because the increased surface area can efficiently promote their (photo)electrochemical performance.^[7,16–20] However, these general synthesis methods (e.g., hydrothermal synthesis, chemical vapor deposition, chemical exfoliation, etc.) suffer from the limitation of the complicated synthesis process, poor film thickness control and uniform coverage on high aspect ratio structures,^[17,19,20,24,25] which seriously suppress the investigation and promotion of

1. Introduction

Molybdenum disulfide (MoS₂), with an intrinsic semiconducting property, has attracted considerable interest and has been widely applied in various areas such as field-effect transistors, phototransistors, gas sensors, and (photo)electrocatalysts.^[1–7] Particularly, MoS₂ has become a desirable candidate in photoelectrochemical (PEC) applications due to its tunable bandgap and excellent visible light-harvesting ability.^[6,8–11] Besides pure MoS₂,^[6] plenty of MoS₂-based heterostructures, like MoS₂/ZnO,^[12] MoS₂/WS₂,^[13] MoS₂/WSe₂^[14] and

C. Shen, E. Wierzbicka, N. Pinna
Institut für Chemie und IRIS Adlershof
Humboldt-Universität zu Berlin
Brook-Taylor-Str. 2, 12489 Berlin, Germany
E-mail: ewa.wierzbicka@hu-berlin.de; nicola.pinna@hu-berlin.de

 The ORCID identification number(s) for the author(s) of this article can be found under <https://doi.org/10.1002/admi.202200643>.

© 2022 The Authors. Advanced Materials Interfaces published by Wiley-VCH GmbH. This is an open access article under the terms of the Creative Commons Attribution-NonCommercial-NoDerivs License, which permits use and distribution in any medium, provided the original work is properly cited, the use is non-commercial and no modifications or adaptations are made.

E. Wierzbicka
Department of Functional Materials and Hydrogen Technology
Faculty of Advanced Technologies and Chemistry
Military University of Technology
2 Kaliskiego Street, Warsaw 00908, Poland

T. Schultz, R. Wang, N. Koch
Institut für Physik und IRIS Adlershof
Humboldt-Universität zu Berlin
Brook-Taylor-Str. 6, 12489 Berlin, Germany

T. Schultz, N. Koch
Helmholtz-Zentrum Berlin für Materialien und Energie GmbH
Hahn-Meitner-Platz 1, 14109 Berlin, Germany

DOI: 10.1002/admi.202200643

the catalytic properties of MoS₂.^[26] Therefore, it is extremely meaningful and challenging to deposit well-controlled MoS₂ onto high aspect ratio nanostructured substrates for promoted PEC performance.

Atomic layer deposition (ALD), an advanced film deposition technique, has attracted great interest in preparing high-quality films such as metal oxides, nitrides, and chalcogenides because of its high conformality and precise control of film thickness.^[27,28] Compared to other synthesis routes, ALD shows great advantages in depositing high-quality films onto complex nanostructures with uniform coverage due to its self-limiting surface reactions.^[27] Up to now, MoS₂ has been fabricated by ALD with different metal precursors, such as Mo(CO)₆,^[29–31] MoCl₅,^[32] Mo(thd)₃ (thd = 2,2,6,6-tetramethylheptane-3,5-dionato),^[33] tetrakis(dimethylamino)molybdenum ((NMe₂)₄Mo),^[34] and bis(*t*-butylimino)bis(dimethylamino)molybdenum ((N^tBu)₂(NMe₂)₂Mo).^[35] The chemisorption of a molybdenum precursor species onto the surface is critical for the second ALD half-reaction. However, incomplete coverage during the metal precursor half-reaction is often attributed to a limited number of reactive sites on the surface and the steric hindrance of chemisorbed precursors on adjacent active sites. In some cases, pre-treatment or enrichment of the surface-active species is essential for improving ALD processes.^[36,37] Thus, precursors which promote facile adsorption onto substrates may greatly improve ALD processes.^[38]

Mo(CO)₆ is one of the most commonly used Mo precursors for ALD, given its high volatility at low temperatures and small ligands. In addition, facile chemisorption of Mo(CO)₆ proceeds via a series of decarbonylation reactions to yield the subcarbonyl surface species Mo(CO)_x (*x* ≤ 5), which can occur even at room temperature.^[39,40] Due to the excellent surface coverage of the chemisorbed Mo(CO)_x and small steric hindrance caused by carbonyl ligands, the ALD processes for MoS₂ films from Mo(CO)₆ show high growth per cycle (GPC) of up to 0.11 nm at as low temperature as 155 °C.^[29,41,42] However, the low thermal stability of Mo(CO)₆ results in a narrow ALD window of 155–175 °C, which restricts its use in practical applications, particularly in preparing multinary dichalcogenides compounds like Mo_xW_{1–x}S₂.^[30,31,42–44] Compared to the carbonyl group, the Mo complexes with some alternative ligands such as alkylamides and diketonates show efficiently improved thermal stability, thus broadening the ALD window. For example, the ALD of MoS₂ from (N^tBu)₂(NMe₂)₂Mo exhibits a broad ALD window of 125–225 °C and 275–350 °C for that from Mo(thd)₃.^[33,45] However, these precursors exhibit lower growth per cycle (0.08 nm for (N^tBu)₂(NMe₂)₂Mo and 0.0025 nm for Mo(thd)₃), which can be ascribed to the lower density of precursor molecules in the chemisorption layer.^[38] Therefore, we come up with the idea that a heteroleptic molybdenum precursor bearing both carbonyl and substitutive ligands may be a promising ALD precursor since it integrates properties of both facile adsorption and better thermal stability.

Ideal representatives are heteroleptic complexes composed of both carbonyl and cycloalkene ligands, which possess better thermal stability and higher volatility than the components containing only carbonyl groups.^[46–48] Therefore, molybdenum complexes with these ligands have been considered as good candidates for the ALD of molybdenum oxides and

nitrides.^[48] For instance, cycloheptatriene molybdenum tricarbonyl (C₇H₈Mo(CO)₃), a heteroleptic molybdenum carbonyl complex with cycloalkene ligand,^[49,50] has been applied for the vapor synthesis of MoO₃ at low temperature (100 °C) due to its high volatility, indicating a good potential for applying as ALD precursor.^[51]

Herein, a low-temperature ALD process was demonstrated for the deposition of MoS₂ from C₇H₈Mo(CO)₃ and H₂S, respectively. Besides planar substrates (e.g., Si, 350 nm thermally oxidized SiO₂/Si, sapphire wafer, and glass), MoS₂ was also successfully deposited onto high aspect ratio substrates such as carbon nanotubes (CNTs) and anodized titanium dioxide nanotube arrays (TiNTs). The crystallinity and purity of the as-deposited MoS₂ films are efficiently improved by an in situ post-deposition sulfurization at 300 °C with H₂S. Furthermore, MoS₂/TiNTs heterostructures exhibit a trifold enhanced photoelectrochemical performance under visible light irradiation compared to pristine TiNTs. Compared to visible light irradiation, the heterostructures also display an improved PEC performance under UV excitation, but within a lower number of optimal ALD cycles applied for the highest PEC performance since they exhibit different excitation models and charge-transfer pathways. Finally, the electronic structure of the MoS₂/TiNT heterostructures and the charge-transfer mechanisms are systematically discussed.

2. Results and Discussion

2.1. MoS₂ ALD Process Development

The ALD process was systematically studied in a homemade ALD reactor at a temperature ranging between 175 and 300 °C. CNTs, Si wafer, thermally oxidized SiO₂/Si wafer, sapphire, and glass were utilized as substrates for the deposition. **Figure 1a** shows the thickness of the deposited films on the Si wafer for 100 ALD cycles as a function of the reaction temperature. For the reaction temperature of 175 °C, there is almost no MoS₂ deposition, which could be attributed to slow reaction thermodynamics between C₇H₈Mo(CO)₃ and H₂S at such a low temperature. While the temperature increases, the film thickness increases to 3 nm at 200 °C, and ≈9 nm at 225 °C for 100 ALD cycles. Then it stays constant at ≈9 nm until the reaction temperature reaches 285 °C, indicating an optimal ALD window for the reaction between 225 and 285 °C. While temperature further increases up to 300 °C, the film thickness decreases, probably on account of the desorption of the precursors from the substrates. The MoS₂ films deposited onto thermally oxidized SiO₂/Si wafers at varying temperatures were investigated by atomic force microscopy (AFM, **Figure S1**, Supporting Information). The AFM results show that the as-deposited films exhibit a low root-mean-square surface roughness of ≈2 nm for the films deposited at 250 °C (**Figure S2**, Supporting Information), indicating that the deposited films are rather smooth. Therefore, to keep low film roughness, the following ALD process was carried out at 250 °C, at the temperature in the middle of the ALD window.

The dose and exposure time of the precursors were further studied at 250 °C. **Figure 1b** presents the relationship between

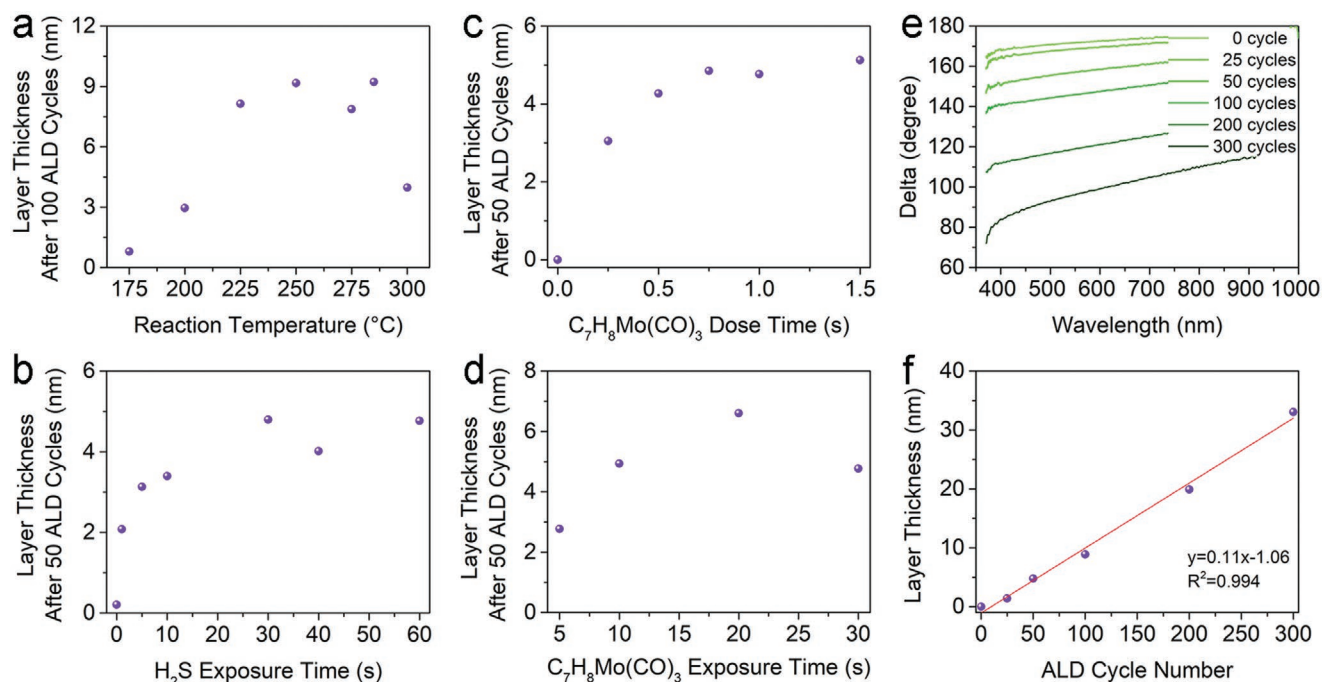


Figure 1. a) The film thickness of the MoS₂ film deposited at different temperatures ranging from 175 to 300 °C. The thickness of 50 ALD cycles MoS₂ film as a function of the b) H₂S exposure time, c) dose time, and d) exposure time of C₇H₈Mo(CO)₃. e) Spectroscopic ellipsometry curves for MoS₂ films deposited with varying ALD cycles (25, 50, 100, 200, and 300). f) There is a linear dependence between the number of ALD cycles and the deposited film thickness. The ALD reaction temperature was 250 °C for all parameter variations except (a).

the film thickness with 50 ALD cycles as a function of the H₂S exposure time, which varied from 0 to 60 s. The results suggest that the second half-reaction is saturated when the exposure time of H₂S was set to 30 s. Figure 1c,d shows the effect of dose and exposure time of C₇H₈Mo(CO)₃ on the film thickness after 50 ALD cycles. The results indicate that a minimum dose time of 0.75 s (Figure 1c) and exposure time of 10 s for C₇H₈Mo(CO)₃ are required to complete the self-limiting surface reaction during the first half cycle (Figure 1d). Considering the

large steric requirements of the metal precursor and the slow saturation, the optimal ALD parameters, dose/exposure/purge time, have been defined as 1.5 s/40 s/30 s for C₇H₈Mo(CO)₃ and 0.2 s/30 s/30 s for H₂S, respectively.

The relationship between film thickness and the number of ALD cycles at 250 °C is shown in Figure 1e,f. Figure 1e shows the original spectroscopic ellipsometry data recorded on natively oxidized Si wafers. The curves gradually shift to lower delta values with the increase of the ALD cycles, indicating an increase in the film thickness. The film thickness increases linearly (R² = 0.99) with a growth per cycle (GPC) of 0.11 nm (Figure 1f). All in all, the results presented in Figure 1 demonstrate angstrom-scale control of the thickness of the films deposited with our new process and its self-limiting nature. Noticeably, the GPC of this novel process is higher than the GPC we recently reported for MoS₂ from (NⁱBu)₂(NMe)₂Mo and H₂S (0.08 nm).^[45] Additionally, MoS₂ films were successfully deposited with the established ALD process on a glass substrate with an area of 5 × 2.5 cm², indicating the potential for large-scale fabrication (Figure S3, Supporting Information).

The chemical composition of the as-deposited films was investigated by X-ray photoelectron spectroscopy (XPS). A typical survey spectrum shown in Figure S4 (Supporting Information) confirms the presence of oxygen, molybdenum, carbon, sulfur in the sample, and silicon from the underlying substrate. The Mo 3d spectra consist of one doublet at ≈229 and ≈232 eV with a 3.15 eV separation, corresponding to Mo⁴⁺ (Figure 2a).^[52] A second doublet at ≈233 and 236 eV can be assigned to the Mo⁶⁺ of MoO₃. This higher BE peak is more pronounced in the films deposited at 250 and 275 °C, which could be attributed to the increased

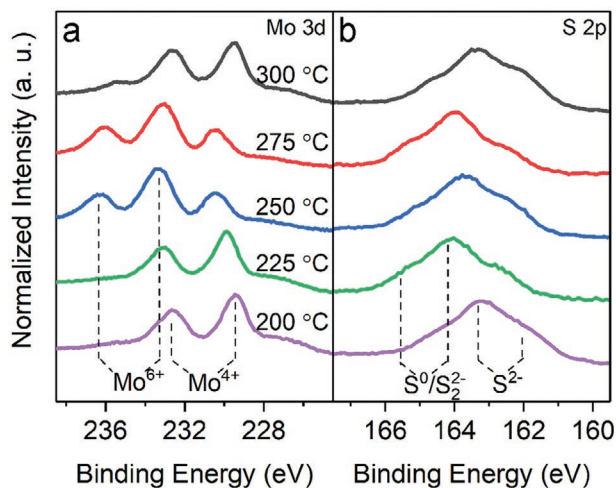
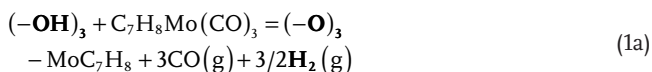


Figure 2. XPS spectra of a) Mo 3d and b) S 2p for the MoS₂ films deposited on SiO₂ at varying temperatures. The different oxidation states and compounds are indicated by dashed lines.

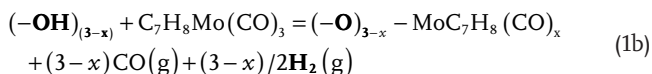
surface roughness (Figures S1 and S2, Supporting Information) that could lead to faster oxidation of the as-deposited film when it is exposed to air. The S 2p spectra suggest that the as-deposited films contain a larger amount of S₂²⁻ or S⁰ species (Figure 2b), which indicates the presence of amorphous MoS₃ or unreacted sulfur,^[9,48] similar to MoS₂ previously grown by low-temperature ALD.^[43,45,53] Furthermore, the C 1s spectra of the deposited films were recorded before and after Ar sputtering, as shown in Figure S5 (Supporting Information). All samples show carbon on the surface of the films, whilst almost no carbon signal can be observed after sputtering. This indicates that the ligands of C₇H₈Mo(CO)₃ were entirely removed during the ALD process, and the detected carbon is typical surface contamination.

Based on the growth parameters, self-limiting nature of the process, and available inorganic chemistry literature on molybdenum complexes, we propose a growth mechanism to further understand the potential of our new ALD process.^[30,46,54]

First, C₇H₈Mo(CO)₃ chemisorbs on the surface of pristine substrates (here depicted as –OH species) or onto the growing MoS_x, similar to most ALD reactions using Mo(CO)₆ as molybdenum precursor, resulting in a substituted molybdenum surface species,

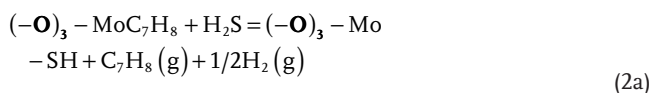


or

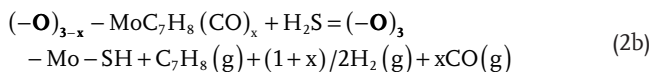


Here, the black –OH group refers to the active site on the initial surface of substrates.

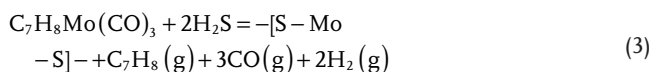
Then, the rest organic ligands are fully released when the co-reactant H₂S reacts with the adsorbed surface species and then producing MoS_x. Thermodynamics calculations have indicated that the reaction of H₂S with various valence molybdenum species (e.g., metallic Mo and MoO₃) under our experimental conditions has a negative Gibbs free energy, suggesting a thermodynamically favorable process.^[55] Therefore, the second half-reaction could be proposed as



or



The full reaction for the ALD process is expected as follows



The hypothesized mechanism is proposed under the following considerations. First, the absorption of molybdenum components on the surface is critical for the full ALD reaction. It has been demonstrated that Mo(CO)₆ is easily physisorbed on surfaces and decarbonylated to form chemisorbed molybdenum subcarbonyls.^[30,39] The CO group is easily disassociated from the adsorbed surface molybdenum components at a relatively low temperature (150–170 °C).^[54] Second, Si(CH₃)₃CpMo(CO)₂(η³-2-methylallyl), a molybdenum carbonyl precursor with a similar structure as C₇H₈Mo(CO)₃, has been demonstrated for MoO₃ deposition by ALD at a reaction temperature of 250 °C.^[46] In that reaction, carbonyl groups and η³-2-methylallyl are released during the first half-reaction whilst the Si(CH₃)₃Cp is removed after O₃ exposures, forming Mo(=O)₂ bonds. This result may reflect that the carbonyl ligand is more easily released from the metal components than the cycloalkene ligand during the first ALD half-reaction. Third, the bond between Mo and the cycloheptatriene group is stronger than between Mo and the carbonyl group. The disassociated energy of the molybdenum-cycloheptatriene bond is 251 kJ mol⁻¹, which is higher than that of 152 kJ mol⁻¹ for a molybdenum-carbonyl bond, indicating that the CO ligand is more easily released than cycloheptatriene.^[47] This also explains why the ALD window for the reaction of C₇H₈Mo(CO)₃ and H₂S is higher than that of Mo(CO)₆ and H₂S.^[42] Therefore, we hypothesize that the CO groups are preferentially released during the first half-reaction (chemisorption of the molybdenum complex), and the cycloheptatriene ligand is removed during the second half-reaction (H₂S exposure). An in situ FT-IR study for the elucidation of the reaction mechanism will be carried out in a follow-up study.

The broad, multi-component S 2p core-level X-ray photoemission spectra reflect that the as-deposited MoS₂ films are of low quality and contain an amount of amorphous species (Figure 2b), which is further evidenced by Raman spectroscopy. There is no pronounced Raman peak of MoS₂ observable in the as-deposited films (Figure S6, Supporting Information), which may suggest a low MoS₂ film crystallinity or the predominant presence of amorphous MoS₃, in line with the XPS results. Post-annealing at a relatively low temperature with H₂S has been proven to be an efficient route to improve the crystallinity of the as-deposited ALD-chalcogenide films.^[45,56] Therefore, an in situ post-annealing with H₂S was carried out at 300 °C for 4 h to increase the crystallinity of the deposited films. Different from the as-deposited films, two characteristic Raman peaks at 406.7 and 380.6 cm⁻¹, corresponding to the A_{1g} and E_{2g} peaks of MoS₂, are observed in the sulfurized films, indicating improved crystallinity of the as-deposited MoS₂ films after post-deposition annealing (Figure S6, Supporting Information). The peak distance of ≈26 cm⁻¹ suggests that the film comprises more than six monolayers.^[57] The same phenomenon was observed in the film deposited on sapphire substrates (Figure S6, Supporting Information). Noticeably, an experiment in which H₂S was replaced with an inert gas (N₂) shows that the H₂S atmosphere is critical to conducting the conversion reaction to pure MoS₂ and improving the crystallinity of the films at the mild temperature sulfurization (Figure S7, Supporting Information).

The sulfurized film was also characterized by XPS to further understand the influence of the in situ post-deposition annealing process. Compared to the as-deposited film, only

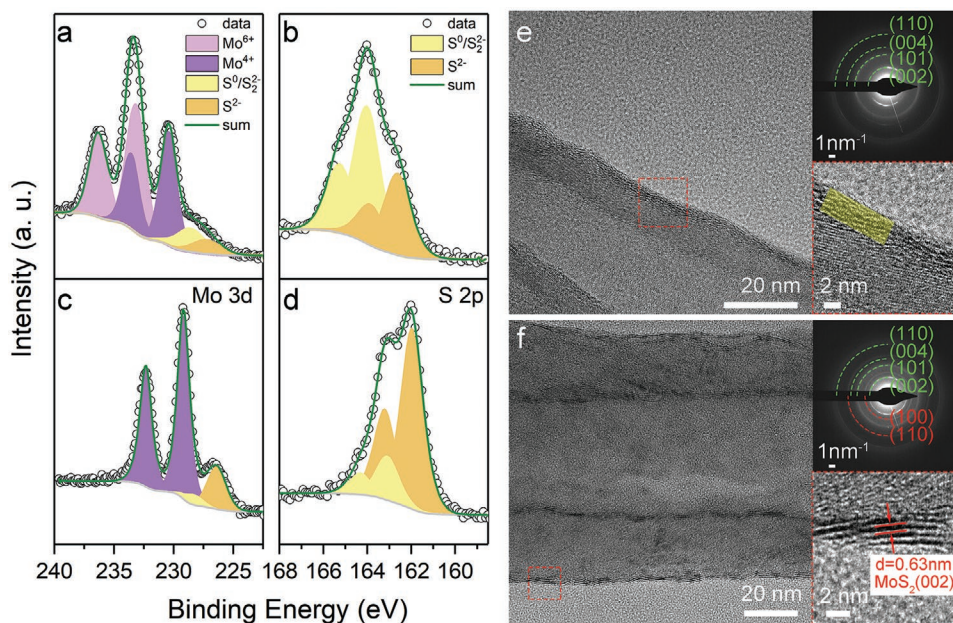


Figure 3. XPS spectra of a,c) Mo 3d and b,d) S 2p for the as-deposited MoS₂ film on SiO₂ a,b) before and c,d) after in situ sulfuration at 300 °C with H₂S. TEM images (left and right down) and SAED pattern (right up) of MoS₂ deposited onto CNTs e) before and f) after in situ sulfuration at 300 °C with H₂S. The green arcs indicate graphite carbon, while the red ones indicate the 2H MoS₂. The yellow mark in (e) suggests the as-deposited amorphous MoS₂ film, while the lattice fringes in (f) suggest the (002) plane of crystalline MoS₂ layers.

one sharp doublet of Mo 3d at 229.2 eV can be observed in the annealed film, which is ascribed to Mo⁴⁺ in MoS₂, in agreement with the literature.^[26] The disappearance of Mo⁶⁺ components at higher binding energies suggests that all Mo was fully converted to Mo⁴⁺ in MoS₂ by post sulfuration (Figure 3c). The same trend is observed in the S 2p spectrum. In contrast to the broad S 2p spectrum in the as-deposited films, here, the pronounced doublet peak at 162.0 eV (S 2p_{3/2}) and 163.2 eV (S 2p_{1/2}) corresponds to the plane S²⁻ in MoS₂ (Figure 3d). The S₂⁻/S⁰ peaks corresponding to amorphous MoS₃ or unreacted sulfur are strongly reduced and can be entirely removed at higher annealing temperatures (Figure S8, Supporting Information).

After optimizing the growth conditions on smooth and planar substrates, the growth of MoS₂ onto nanostructured substrates with high aspect ratios was further investigated. A prototypical representative of these materials is carbon nanotubes (CNTs). To examine the morphology of the MoS₂ film and the influence of the post-annealing process, the MoS₂ films deposited onto CNTs were characterized by high-resolution transmission electron microscopy (HR-TEM) and selected area electron diffraction (SAED). Although both CNTs are entirely coated with a smooth film, the SAED patterns suggest that the as-deposited MoS₂ film is amorphous (Figure 3e), while the film after post-deposition sulfuration is polycrystalline (Figure 3f). Moreover, compared with the as-deposited amorphous films (light yellow mark in Figure 3e, right down), the sulfurized films exhibit clear lattice fringes associated with a d-spacing of 0.63 nm, which are assigned to the (002) planes of MoS₂ (Figure 3f, right down). Consequently, all of the above results evidence the successful deposition of high conformal MoS₂ by ALD at relatively low temperatures (<300 °C) using C₇H₈Mo(CO)₃ and H₂S as precursors, with an improved film purity and crystallinity

obtained by the following in situ post-deposition sulfuration at 300 °C with H₂S. Moreover, the successful development of this ALD process suggests that heteroleptic cycloalkenes metal carbonyl complexes can be considered as promising metal precursors for the ALD of metal chalcogenides.

2.2. MoS₂ Coated TiO₂ Nanotubes for Photoelectrochemical Applications

Our novel ALD process has been applied to synthesize MoS₂/TiO₂ heterojunctions and elucidate their PEC performance. As discussed in the introduction, MoS₂/TiO₂ heterostructure constructed by combining TiO₂ nanotubes and ALD-MoS₂ is expected to be an efficient photoelectrode. Figure 4a schematically illustrates the archetypical fabrication process of ALD-MoS₂/TiO₂ nanotube array (denoted as MoS₂/TiNTs) heterostructures constructed by depositing MoS₂ onto TiO₂ nanotube arrays (marked as TiNTs) with the established ALD process. Figure 4b,c shows the scanning electron microscopy (SEM) top view of the anodized TiO₂ nanotube arrays before (Figure 4b) and after coating with 200 ALD cycles of MoS₂ (Figure 4c). SEM cross-section images are shown in Figure S9 (Supporting Information). Both samples show similar morphology but significantly decreased pore diameters, with the average hole diameter decreasing from 62 nm for pristine TiNTs to 54 nm for MoS₂/TiNTs (Figure S10, Supporting Information).

The composition of the TiNTs substrates before and after ALD-MoS₂ coating was confirmed by Raman spectroscopy, shown in Figure 4d. For the pristine TiNTs sample, the intense Raman peak at ≈144 cm⁻¹ and three strong vibrational peaks

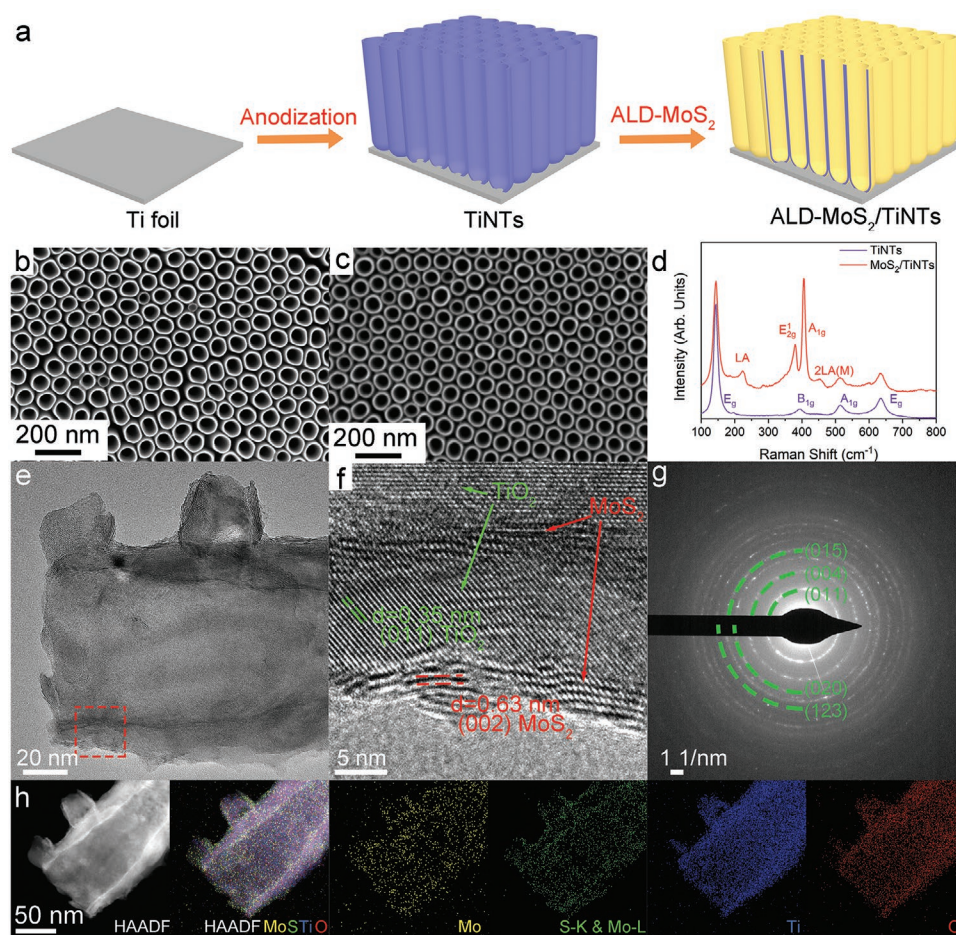


Figure 4. a) Schematic illustration of the fabrication process for the $\text{MoS}_2/\text{TiNTs}$ heterostructure. SEM images of TiNTs top-view b) before and c) after 200 ALD- MoS_2 coating. d) Raman spectrum of the TiNTs before and after ALD- MoS_2 deposition. e, f) TEM and high-resolution TEM images, g) SAED, and h) HAADF-STEM and EDX element mapping of $\text{MoS}_2/\text{TiNTs}$ heterostructure.

observed at 394, 515, and 635 cm^{-1} can be assigned to E_{1g} , B_{1g} , A_{1g} , and E_g vibration modes of anatase TiO_2 , respectively. Apart from the signal of anatase TiO_2 , the $\text{MoS}_2/\text{TiNTs}$ sample shows two characteristic Raman peaks of A_{1g} and E_{2g}^1 vibration modes of MoS_2 at ≈ 408 and 382 cm^{-1} , suggesting the successful deposition of ALD- MoS_2 onto TiNTs. The morphology and structure of $\text{MoS}_2/\text{TiNTs}$ were further demonstrated by TEM. After ALD, the TiO_2 nanotubes were homogeneously coated with MoS_2 inside and outside (Figure 4e,f; Figure S11, Supporting Information). The clear lattice fringes of 0.63 and 0.35 nm reflect the (002) planes of MoS_2 and the (101) planes of anatase TiO_2 (Figure 4f), respectively. The SAED pattern of $\text{MoS}_2/\text{TiNTs}$ (Figure 4g) indicates that the TiO_2 is polycrystalline. No obvious diffraction signal assigned to MoS_2 can be observed from the pattern due to the low mass loading of MoS_2 and strong diffraction of TiO_2 . However, strong S and Mo signals from MoS_2 are observed on the energy-dispersive X-ray spectroscopy (EDX) spectrum (Figure S12, Supporting Information). The high-angle annular dark-field scanning transmission electron microscopy (HAADF-STEM) images and the corresponding element maps, as shown in Figure 4h, further reveal a homogeneous distribution of Mo and S elements throughout the inner and outer TiNTs wall.

The PEC performance of the $\text{MoS}_2/\text{TiNTs}$ electrode was tested to prove the beneficial influence of the heterojunction. A LED visible-light source with 430 nm wavelength (energy lower than TiO_2 bandgap) was applied for the PEC testing to ensure excitation of MoS_2 . The applied potential dependent photocurrent densities of the pristine TiNTs and $\text{MoS}_2/\text{TiNTs}$ (with 200 ALD cycles MoS_2) heterostructure were recorded in the dark and under light irradiation (Figure S13, Supporting Information). The registered responses show that both electrodes excited under the 430 nm LED irradiation are stable in the whole potential range, and that the $\text{MoS}_2/\text{TiNTs}$ heterostructure exhibits significantly enhanced PEC performance than the pure TiNTs. Figure 5a shows the chopped photocurrent density versus time curves of the pristine TiNTs and $\text{MoS}_2/\text{TiNTs}$ heterostructure with an external bias potential of 0.5 V. The $\text{MoS}_2/\text{TiNTs}$ heterostructure displays an improved photocurrent density of $\approx 30\text{ }\mu\text{A cm}^{-2}$, corresponding to an incident-photon-to-current-conversion efficiency (IPCE) of $\approx 0.247\%$, which is three times higher than pristine TiNTs (photocurrent density of $\approx 10\text{ }\mu\text{A cm}^{-2}$ and IPCE of $\approx 0.082\%$). The significant improvement in the photocurrent density of the $\text{MoS}_2/\text{TiNTs}$ heterostructure could be attributed to the enhanced visible light-harvesting of MoS_2 and further evidence the successful

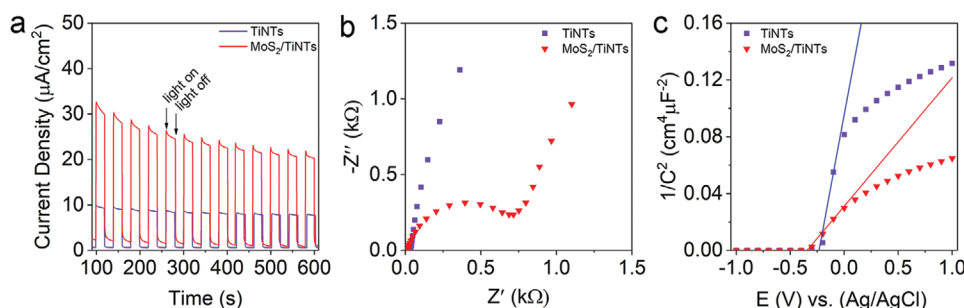


Figure 5. a) Photocurrent density and response of the TiNTs (purple) and MoS₂/TiNTs (red, with 200 ALD cycles MoS₂ deposition). The photocurrent was recorded in 0.5 M Na₂SO₄ electrolyte with a 0.5 V external bias potential in the dark and under 430 nm light irradiation. b) Nyquist and c) Mott–Schottky plots of TiNTs (purple) and MoS₂/TiNTs heterostructure (red). The Nyquist plots were recorded under 430 nm light irradiation.

electron transport through the MoS₂/TiNTs junction. Their PEC stabilities were further evaluated during 80 min long experiment (Figure S14, Supporting Information). Although MoS₂/TiNTs electrode depicts some degradation in the first 40 min of the process, after that the efficiency stabilizes and photocurrents of around 15 $\mu\text{A cm}^{-2}$ are maintained. Clearly, even in the long-time testing, the heterostructure generates more than twice times higher photocurrents than the pristine TiNTs.

Furthermore, a strong correlation has been found between the PEC performance and the number of ALD cycles, ultimately the mass loading of the MoS₂ (Figure S15, Supporting Information). Under the visible light (430 nm) illumination, the best PEC performance was obtained for the samples with 100 and 200 ALD cycles of MoS₂, where the latter shows better stability. In contrast, the samples with either fewer ALD cycles of MoS₂ (50 ALD cycles) or more ALD cycles (300 ALD cycles) are less stable/efficient. This reflects the optimal tradeoff between the thickness of the light-absorbing layer to collect all incident light and the distance for photo-generated charges to travel through the material (for details, see Supporting Information).

In the next PEC experiment, a UV light source (LED 365 nm) was used to test the photoanodes properties (Figure S16, Supporting Information). The excitation energy is high enough to excite titanium dioxide (≈ 3.2 eV for anatase).^[58] As shown in Figure S16 (Supporting Information), the presence of MoS₂ also positively influences PEC light conversion in the UV range. However, the highest performance (1.12 mA cm⁻², 22.44% of IPCE) has already been reached after 5 ALD cycles of MoS₂. Compared to the MoS₂/TiO₂ heterostructure prepared by other methods for PEC application (Table S1, Supporting Information), our system shows outstanding performance in PEC water splitting reflected in high photocurrents exhibited. The beneficial influence of the deposited MoS₂ on the PEC process is attributed to a suitable band alignment of both semiconductors that facilitate the separation of photo-generated charge carriers (discussed in detail in the following section). Moreover, it is feasible that the oxidation reaction might occur with higher efficiency at the surface of MoS₂ instead of TiO₂ since the potential energy of holes in MoS₂ is much closer to the water oxidation potential. On the other hand, the optimal thickness of MoS₂ is much lower than in the case of visible light excitation because the shading effect of MoS₂ hinders UV light absorption by the internal TiO₂ layer.

As discussed above, the improved PEC performance might be attributed to the efficient charge separation between the two semiconductors in the MoS₂/TiNTs heterostructure.^[19] This hypothesis is further supported by electrochemical impedance spectroscopy (EIS). As shown in Figure 5b and Figure S17 (Supporting Information), the Nyquist plot of MoS₂/TiNTs exhibits a clear semicircle with a lower radius than that of unmodified TiNTs, indicating significantly lower charge transport resistance and facilitated charge separation in the MoS₂/TiNTs heterostructure.^[12,59,60]

To further understand the reason for the improved PEC performance of heterojunction electrodes, Mott–Schottky (M–S) measurements were conducted. As shown from the plots in Figure 5c, both TiNTs and MoS₂/TiNTs components display a positive slope in M–S plots, indicating n-type conductivity. Moreover, the plot of MoS₂/TiNTs in Figure 5c depicts a suppressed slope compared to pristine TiNTs, suggesting a higher carrier concentration in the heterostructure than in the pure TiNTs.^[59,61] These results, together with EIS analysis, further evidence that not only visible light absorption is the reason for the improvement of PEC performance of heterojunction-based photoanode, but also the increased charge carriers density and lower resistance provided by the presence of MoS₂.

The band alignment of the two semiconductors plays a vital role in the charge transfer mechanisms and therefore affects the PEC performance. Ultraviolet photoelectron (UPS) and XPS spectra were acquired to determine the exact band offsets. It is significant for MoS₂ since the size-related quantum confinement effects can alter the bandgap, and therefore simply considering literature values might lead to wrong conclusions.^[9,60] The secondary electron cutoffs (SECOs) were determined as 4.92 and 5.15 eV for TiNTs and MoS₂/TiNTs, respectively (Figure 6a), indicating a 0.23 eV increase of the work function ($\Delta\Phi$). After MoS₂ ALD, the Ti 2p_{3/2} core-level shifts to lower binding energy by 0.20 eV (Figure 6b), suggesting an upward band bending ($\Delta\Phi_{\text{BB}} = 0.20$ eV). The UPS spectra reveal that the valence band maximum (E_{VBM}) of TiO₂ is located at 3.1 eV (below the Fermi level, E_{F}), while the E_{VBM} of MoS₂ is located at 1.1 eV (Figure 6c,d). The obtained results are summarized in a band diagram for the formed heterojunction (Figure 6e), resulting in a type II heterostructure. This means that when both TiO₂ and MoS₂ are excited, the photo-generated electrons in the CBM of MoS₂ will transfer to the CBM of TiO₂ and then to the external circuit, whilst the photo-generated holes in the

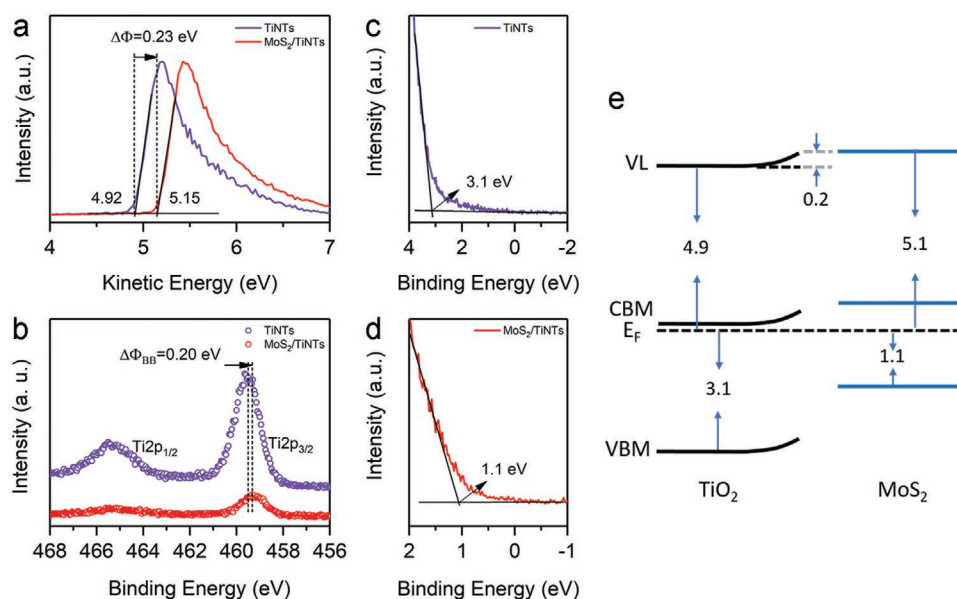


Figure 6. a) Secondary electron cutoff and b) Ti 2p spectra of TiNTs (violet) and MoS₂/TiNTs (red). Valence band spectra of c) TiNTs and d) MoS₂/TiNTs. e) Band diagram of the MoS₂/TiNTs heterojunction.

VBM of TiO₂ will transfer to the VBM of MoS₂ for the oxidation reaction (Figure S18, Supporting Information). Therefore, the charge separation is facilitated, ultimately resulting in improved photoelectrochemical performance.

3. Conclusion

In summary, C₇H₈Mo(CO)₃ is successfully employed as a molybdenum precursor for the ALD of MoS₂ at low temperatures, combined with H₂S as a sulfur source. This process shows a growth per cycle rate of ≈ 0.11 nm within an ALD window of 225–285 °C. XPS characterization suggests that the as-deposited MoS₂ films are amorphous with a complete exchange or removal of the carbon-containing ligands during the ALD process. The crystallinity and chemical purity of the as-deposited MoS₂ films are efficiently improved by in situ post-deposition annealing in the ALD chamber at 300 °C under an H₂S atmosphere. These observations suggest that heteroleptic cycloalkene carbonyl metal complexes should be considered as one type of promising precursors for the ALD of metal chalcogenides. Moreover, the practical application of the established ALD process is demonstrated by fabricating MoS₂/TiNTs heterostructures for photoelectrochemical water splitting. The enhanced visible light-harvesting ability, increased carrier concentration, and lower charge transfer resistance of MoS₂/TiNTs in comparison to pristine TiNTs, result in three times higher PEC performances. UPS and XPS studies confirm the type-II band alignment of the heterostructure, which supports the separation of photo-generated charges. We believe that this work will stimulate more research on establishing novel ALD processes for metal chalcogenides by using heteroleptic cycloalkene carbonyl metal complexes and employing ALD in photoelectrocatalysis applications.

4. Experimental Section

ALD-MoS₂: The nitric acid-treated CNTs were dispersed into ethanol with sufficient sonication and drop-casted onto aluminum foil for MoS₂ deposition.^[45] The (cycloheptatriene) molybdenum tricarbonyl (C₇H₈Mo(CO)₃, 99.0%, Strem) was stored in a stainless steel cylinder (kept at 30 °C) as the molybdenum precursor for the MoS₂ deposition and H₂S (Air Liquide, CAS number: 7783-06-4, H₂S > 99.5%) was used as sulfur source with a pressure of 400 mbar. The MoS₂ deposition was carried out in a homemade ALD reactor with N₂ (Air Liquide, 99.99%) as carrying and purging gas. Functionalized CNTs, 350 nm thermal SiO₂/Si wafer, Si wafer, sapphire, and glass were used as substrates, where the oxidized CNTs were used to perform the TEM, the silicon wafers were used to optimize the ALD parameters, and the silica wafers were used to characterize XPS. The optical characterizations were performed on SiO₂/Si wafer and glass. The ALD reaction contained dose/exposure/purge processes with a time of 1 s/30 s/30 s for C₇H₈Mo(CO)₃ and 0.2 s/30 s/30 s for H₂S, respectively, unless otherwise stated. The dose and exposure time for precursors were varied to study and optimize this ALD reaction by fixing other parameters. The ALD reactions happened under a temperature ranging from 200–300 °C. The pneumatic valves were kept at 110 °C to avoid condensation of the metal precursor during the ALD reaction.

Post-Sulfurization: The as-deposited MoS₂ films were in situ sulfurized in the ALD chamber at 300 °C with H₂S dose followed by the ALD deposition. The H₂S dose process contained a dose/exposure/purge time of 0.2 s/60 s/30 s for 160 cycles (indicating 4 h). To further understand the influence of the post-sulfurization, the as-deposited MoS₂ films were post-sulfurized in a tube furnace with sulfur powder. The sulfurized temperature was set as 700 °C with a ramp of 10 °C min⁻¹. Ar (Air Liquide, 99.99%) was used as carry gas. Before increasing the temperature to 700 °C, the tube was purged with Ar for 30 min to remove residual air.

Synthesis of TiO₂ Nanotubes: TiO₂ nanotubes were prepared by self-organized anodizing of a Ti substrate (Advent, 0.125 mm thickness, purity > 99.6%). Before anodizing, the titanium substrates were degreased by sonication subsequently in acetone, ethanol, and deionized water (15 min for each solvent), followed by drying in a nitrogen stream. Anodizing was a two-step procedure. The first step was carried out in 3 M of HF (48% purity, Sigma-Aldrich) prepared in

melted $\text{o-H}_3\text{PO}_4$. Before anodizing, the electrolyte was kept at 100 °C for 30 min to reduce the water content. The temperature was maintained at 100 °C during anodizing. The first step of the process was carried out for 3 h at 17 V using a power supply in a two-electrode cell with a platinum counter electrode. The second anodizing step was conducted in ethylene glycol-based (Sigma–Aldrich) electrolyte consisting of deionized water (3% vol.) and NH_4F (0.15 M, Sigma–Aldrich, 98%) for 1 min at 60 V. This sequential procedure was applied to ensure the open-pores structure of TiO_2 nanotubes. Thermal annealing was performed in a furnace in air at 450 °C for 1 h to convert the amorphous nanotubes layer to anatase.

Synthesis of $\text{MoS}_2/\text{TiNTs}$ Heterostructure: The prepared TiO_2 nanotubes were coated by MoS_2 with the established ALD process at 250 °C to construct the $\text{MoS}_2/\text{TiO}_2$ heterostructure. The dose/exposure/purge of the precursors were set as 1.5 s/40 s/30 s for $\text{C}_2\text{H}_5\text{Mo}(\text{CO})_3$ and 0.2 s/30 s/30 s for H_2S , respectively. The ALD cycles number varied from 0 to 300.

Characterization: The relative thickness of the deposited thin films was determined by spectroscopic ellipsometry (SENpro Sentech). The data were collected under a 70° incidence angle in an energy range from 370–1000 nm. The thickness value was determined by fitting the measured data using the software SpectraRay 4 and assuming a trilayer model (semiconductor/native oxide/Si), where the native oxide on the single Si substrate is ≈ 1.6 nm thick. All the deposited layers are fitted with the same model and parameters. The Raman spectra were collected on an XPLORA plus Raman microscope with a 532 nm laser and calibrated with the phonon mode of Si at 520 cm^{-1} . An FEI Talos F200S system was used for the transmission electron microscopy (TEM) measurements, as well as the high-resolution transmission electron microscopy (HRTEM), high-angle annular dark-field scanning transmission electron microscopy (HAADF-STEM), and energy dispersive X-ray analysis (EDX) measurements. The operation voltage was set to 200 kV. ZEISS MERLIN FE-SEM was operated at an accelerating voltage of 5 kV for the scanning electron microscopy (SEM) recording. X-ray photoelectron spectroscopy (XPS) data were measured at a JEOL JPS-9030 setup (base pressure 10^{-9} mbar), using an Mg X-ray source ($h\nu = 1253.6$ eV) for excitation. A pass energy of 10 eV was used for the narrow scans, yielding an overall setup resolution of 0.8 eV, as determined from the width of an $\text{Ag}3d_{5/2}$ peak (310 meV natural line width assumed). The binding energy scale of the setup was calibrated by setting the $\text{Au}4f_{7/2}$ of a gold foil to 84.0 eV. However, since some of the samples were charging, it was chosen to set the binding energy of the $\text{Si}2p$ peak from the underlying SiO_2 substrate to 103.5 eV for better comparison between the samples.^[62] There is, therefore, refrainment from an interpretation of the exact binding energy values. The samples were sputtered for 10 s at an argon pressure of 3×10^{-4} mbar using the equipped high-rate etching source to remove surface contaminants. The ultra-violet photoelectron spectra (UPS, hydrogen Lyman- α excitation source, $h\nu = 10.2$ eV) were recorded on TiO_2 nanotube arrays before and after ALD- MoS_2 coating. A bias voltage of -10 V was applied for the secondary electron cutoff (SECO) measurements. Atomic force microscopy (AFM) measurements were recorded using a Bruker Dimension Icon in Peak Force Tapping + ScanAsyst mode and ScanAsyst-Air cantilevers.

Photoelectrochemical Measurements: The photoanodes composed of MoS_2 thin films deposited onto the anodized TiO_2 nanotubes array have been used to study the photoelectrochemical (PEC) performance of water splitting in a home-build three-electrode PEC cell with a 0.785 cm^2 working area. A Pt plate ($1 \times 1 \text{ cm}^2$) and Ag/AgCl electrode were applied as counter and reference electrodes, respectively, and 0.5 M Na_2SO_4 solution was used as electrolyte. A 20 min degassing process with Ar flow was carried out to remove the dissolved oxygen in the electrolyte before PEC testing. The PEC measurements were tested under 430 nm (M430L4 Spectrum) and 365 nm (M365L4 Spectrum) LED illumination with a light intensity of 35 and 17 mW cm^{-2} , respectively. The power of the LEDs was measured with Compact Power and Energy Meter (PM100D, Thorlabs). The linear sweep voltammetry (LSV) test was carried with and without irradiation of 430 nm LED at 5 mV s^{-1} . The reversible hydrogen electrode (RHE) potential was calculated according to the Nernst equation:

$$E_{(\text{RHE})} = E_{(\text{Ag}/\text{AgCl})} + 0.059 \times \text{pH} + E_{0(\text{Ag}/\text{AgCl})} \quad (4)$$

where the $E_{(\text{Ag}/\text{AgCl})}$ was measured potential versus Ag/AgCl , $E_{0(\text{Ag}/\text{AgCl})}$ was 0.195 V at 25 °C, and pH is 6.8 in the system.

The photocurrent responses were recorded at 0.5 V bias potential (vs Ag/AgCl) under on–off illumination cycles. EIS measurements were recorded over a frequency range of 0.1 Hz to 10 kHz at an AC bias potential of 5 mV. Mott–Schottky analysis was measured at 1 kHz frequency without irradiation. The incident-photon-to-current-conversion efficiency (IPCE) was calculated according to the following formula

$$\text{IPCE} = \frac{1240 (\text{Vnm}) \times |J_{\text{ph}} (\text{mA cm}^{-2})|}{\lambda (\text{nm}) \times P_{\text{light}} (\text{mW cm}^{-2})} \times 100 \quad (5)$$

where J_{ph} is the photocurrent density, λ is the wavelength of the light source, and P_{light} is the incident irradiance.^[60,63]

Supporting Information

Supporting Information is available from the Wiley Online Library or from the author.

Acknowledgements

C.S. acknowledges the fellowship from the China Scholarship Council (CSC). E.W. thanks the Alexander von Humboldt Foundation, Bonn, Germany, for funding the postdoctoral fellowship. The authors thank C. Erdmann for performing the transmission electron microscopy measurements and J. H. Zhang and J. Müller for the scanning electron microscopy measurements. This work was partially funded by the Deutsche Forschungsgemeinschaft (DFG) – Projektnummer PI 762/11-1, Deutsche Forschungsgemeinschaft (DFG) – Projektnummer 182087777-SFB 951.

Open access funding enabled and organized by Projekt DEAL.

Conflict of Interest

The authors declare no conflict of interest.

Data Availability Statement

The data that support the findings of this study are available from the corresponding author upon reasonable request.

Keywords

atomic layer deposition, solar fuels, titania nanotubes, water splitting

Received: March 22, 2022

Revised: May 2, 2022

Published online: June 17, 2022

- [1] W. Jeon, Y. Cho, S. Jo, J. H. Ahn, S. J. Jeong, *Adv. Mater.* **2017**, *29*, 1703031.
- [2] B. Radisavljevic, A. Radenovic, J. Brivio, V. Giacometti, A. Kis, *Nat. Nanotechnol.* **2011**, *6*, 147.
- [3] F. K. Perkins, A. L. Friedman, E. Cobas, P. M. Campbell, G. G. Jernigan, B. T. Jonker, *Nano Lett.* **2013**, *13*, 668.

- [4] W. Wu, C. Niu, C. Wei, Y. Jia, C. Li, Q. Xu, *Angew. Chem., Int. Ed. Engl.* **2019**, 58, 2029.
- [5] W. Zhang, J. K. Huang, C. H. Chen, Y. H. Chang, Y. J. Cheng, L. J. Li, *Adv. Mater.* **2013**, 25, 3456.
- [6] X. Xu, J. Hu, Z. Yin, C. Xu, *ACS Appl. Mater. Interfaces* **2014**, 6, 5983.
- [7] A. D. Nguyen, T. H. Pham, T. K. Nguyen, H. Ullah, Z. Tahir, Y. C. Park, J. Park, J. I. Jang, Y. H. Shin, Y. S. Kim, *ACS Appl. Energy Mater.* **2020**, 3, 10854.
- [8] Y. Yoon, K. Ganapathi, S. Salahuddin, *Nano Lett.* **2011**, 11, 3768.
- [9] A. M. de Jong, H. J. Borg, L. J. van Ijzendoorn, V. G. F. M. Soudant, V. H. J. de Beer, J. A. R. van Veen, J. W. Niemantsverdriet, *J. Phys. Chem.* **1993**, 97, 6477.
- [10] J. Joe, H. Yang, C. Bae, H. Shin, *Catalysts* **2019**, 9, 149.
- [11] Z. Yin, B. Chen, M. Bosman, X. Cao, J. Chen, B. Zheng, H. Zhang, *Small* **2014**, 10, 3537.
- [12] T. N. Trung, D.-B. Seo, N. D. Quang, D. Kim, E.-T. Kim, *Electrochim. Acta* **2018**, 260, 150.
- [13] F. M. Pesci, M. S. Sokolikova, C. Grotta, P. C. Sherrell, F. Reale, K. Sharda, N. Ni, P. Palczynski, C. Mattevi, *ACS Catal.* **2017**, 7, 4990.
- [14] J. Xiao, Y. Zhang, H. Chen, N. Xu, S. Deng, *Nano-Micro Lett.* **2018**, 10, 60.
- [15] Y. Liu, Y.-X. Yu, W.-D. Zhang, *J. Phys. Chem. C* **2013**, 117, 12949.
- [16] Y. Y. Li, J. H. Wang, Z. J. Luo, K. Chen, Z. Q. Cheng, L. Ma, S. J. Ding, L. Zhou, Q. Q. Wang, *Sci. Rep.* **2017**, 7, 7178.
- [17] L. Zheng, S. Han, H. Liu, P. Yu, X. Fang, *Small* **2016**, 12, 1527.
- [18] X. Zhou, M. Lickleder, P. Schmuki, *Electrochem. Commun.* **2016**, 73, 33.
- [19] F. Nan, P. Li, J. Li, T. Cai, S. Ju, L. Fang, *J. Phys. Chem. C* **2018**, 122, 15055.
- [20] L. Guo, Z. Yang, K. Marcus, Z. Li, B. Luo, L. Zhou, X. Wang, Y. Du, Y. Yang, *Energy Environ. Sci.* **2018**, 11, 106.
- [21] J. Jeon, S. K. Jang, S. M. Jeon, G. Yoo, Y. H. Jang, J. H. Park, S. Lee, *Nanoscale* **2015**, 7, 1688.
- [22] Q. Xu, Y. Liu, H. Jiang, Y. Hu, H. Liu, C. Li, *Adv. Energy Mater.* **2018**, 9, 1802553.
- [23] Y. Li, H. Wang, L. Xie, Y. Liang, G. Hong, H. Dai, *J. Am. Chem. Soc.* **2011**, 133, 7296.
- [24] D. Fu, X. Zhao, Y. Y. Zhang, L. Li, H. Xu, A. R. Jang, S. I. Yoon, P. Song, S. M. Poh, T. Ren, Z. Ding, W. Fu, T. J. Shin, H. S. Shin, S. T. Pantelides, W. Zhou, K. P. Loh, *J. Am. Chem. Soc.* **2017**, 139, 9392.
- [25] F. Tumino, C. S. Casari, M. Passoni, V. Russo, A. Li Bassi, *Nanoscale Adv.* **2019**, 1, 643.
- [26] B. D. Keller, A. Bertuch, J. Provine, G. Sundaram, N. Ferralis, J. C. Grossman, *Chem. Mater.* **2017**, 29, 2024.
- [27] C. Marichy, M. Bechelany, N. Pinna, *Adv. Mater.* **2012**, 24, 1017.
- [28] A. S. Asundi, J. A. Raiford, S. F. Bent, *ACS Energy Lett.* **2019**, 4, 908.
- [29] D. K. Nandi, S. Sahoo, S. Sinha, S. Yeo, H. Kim, R. N. Bulakhe, J. Heo, J. J. Shim, S. H. Kim, *ACS Appl. Mater. Interfaces* **2017**, 9, 40252.
- [30] Z. Jin, S. Shin, D. H. Kwon, S. J. Han, Y. S. Min, *Nanoscale* **2014**, 6, 14453.
- [31] C. MacIsaac, J. R. Schneider, R. G. Closser, T. R. Hellstern, D. S. Bergsman, J. Park, Y. Liu, R. Sinclair, S. F. Bent, *Adv. Funct. Mater.* **2018**, 28, 1800852.
- [32] T. A. Ho, C. Bae, S. Lee, M. Kim, J. M. Montero-Moreno, J. H. Park, H. Shin, *Chem. Mater.* **2017**, 29, 7604.
- [33] M. Mattinen, T. Hatanpää, T. Sarnet, K. Mizohata, K. Meinander, P. J. King, L. Khriachtchev, J. Räisänen, M. Ritala, M. Leskelä, *Adv. Mater. Interfaces* **2017**, 4, 1700123.
- [34] T. Jurca, M. J. Moody, A. Henning, J. D. Emery, B. Wang, J. M. Tan, T. L. Lohr, L. J. Lauhon, T. J. Marks, *Angew. Chem., Int. Ed. Engl.* **2017**, 56, 4991.
- [35] B. Kalanyan, R. Beams, M. B. Katz, A. V. Davydov, J. E. Maslar, R. K. Kanjolia, *J. Vac. Sci. Technol., A* **2019**, 37, 010901.
- [36] Y. Wu, M. H. Raza, Y.-C. Chen, P. Amsalem, S. Wahl, K. Skrodzky, X. Xu, K. S. Lokare, M. Zhukush, P. Gaval, N. Koch, E. A. Quadrelli, N. Pinna, *Chem. Mater.* **2019**, 31, 1881.
- [37] J. J. P. M. Schulp, M. A. Verheijen, W. M. M. Kessels, V. Vandalon, A. A. Bol, *2D Mater.* **2022**, 9, 025016.
- [38] M. Knez, K. Nielsch, L. Niinistö, *Adv. Mater.* **2007**, 19, 3425.
- [39] K. P. Reddy, T. L. Brown, *J. Am. Chem. Soc.* **1995**, 117, 2845.
- [40] H. H. Huang, C. S. Sreekanth, C. S. Seet, X. Jiang, G. Q. Xu, *Surf. Sci.* **1996**, 365, 769.
- [41] K. A. Gesheva, T. Ivanova, *Chem. Vap. Deposition* **2006**, 12, 231.
- [42] J. J. Pyeon, S. H. Kim, D. S. Jeong, S. H. Baek, C. Y. Kang, J. S. Kim, S. K. Kim, *Nanoscale* **2016**, 8, 10792.
- [43] S. Shin, Z. Jin, D. H. Kwon, R. Bose, Y. S. Min, *Langmuir* **2015**, 31, 1196.
- [44] W. Alfalasi, I. Al Qasir, N. Tit, *New J. Phys.* **2021**, 23, 103027.
- [45] C. Shen, M. H. Raza, P. Amsalem, T. Schultz, N. Koch, N. Pinna, *Nanoscale* **2020**, 12, 20404.
- [46] C. E. Nanayakkara, A. Vega, G. Liu, C. L. Dezelah, R. K. Kanjolia, Y. J. Chabal, *Chem. Mater.* **2016**, 28, 8591.
- [47] J. A. Connor, Springer, Berlin, Heidelberg, **1977**, 71.
- [48] R. Odedra, S. Garratt, M. Saly, R. Kanjolia, SIGMA-ALDRICH CO. LLC, St. Louis, MO (US), US9175023, **2013**.
- [49] I. Ro, I. B. Aragao, Z. J. Brentzel, Y. Liu, K. R. Rivera-Dones, M. R. Ball, D. Zanchet, G. W. Huber, J. A. Dumesic, *Appl. Catal. B* **2018**, 231, 182.
- [50] I. Ro, C. Sener, T. M. Stadelman, M. R. Ball, J. M. Venegas, S. P. Burt, I. Hermans, J. A. Dumesic, G. W. Huber, *J. Catal.* **2016**, 344, 784.
- [51] T. Cui, X. Pan, J. Dong, S. Miao, D. Miao, X. Bao, *Nano Res.* **2018**, 11, 3132.
- [52] Y. Cai, H. Yang, J. Zhou, Z. Luo, G. Fang, S. Liu, A. Pan, S. Liang, *Chem. Eng. J.* **2017**, 327, 522.
- [53] S. Ng, R. Zazpe, J. Rodriguez-Pereira, J. Michalička, J. M. Macak, M. Pumera, *J. Mater. Chem. A* **2021**, 9, 11405.
- [54] L. Zeng, N. E. Richey, D. W. Palm, I.-K. Oh, J. Shi, C. MacIsaac, T. Jaramillo, S. F. Bent, *J. Vac. Sci. Technol., A* **2020**, 38, 060403.
- [55] M. H. Heyne, D. Chiappe, J. Meerschaut, T. Nuytten, T. Conard, H. Bender, C. Huyghebaert, I. P. Radu, M. Caymax, J. F. de Marneffe, E. C. Neyts, S. De Gendt, *J. Mater. Chem. C* **2016**, 4, 1295.
- [56] M. Mattinen, T. Hatanpää, P. J. King, K. Meinander, K. Mizohata, P. Jalkanen, J. Räisänen, M. Ritala, M. Leskelä, *J. Vac. Sci. Technol., A* **2019**, 37, 020921.
- [57] C. Lee, H. Yan, L. E. Brus, T. F. Heinz, J. Hone, S. Ryu, *ACS Nano* **2010**, 4, 2695.
- [58] E. Wierzbicka, X. Zhou, N. Denisov, J. Yoo, D. Fehn, N. Liu, K. Meyer, P. Schmuki, *ChemSusChem* **2019**, 12, 1900.
- [59] A. Ali, F. A. Mangrio, X. Chen, Y. Dai, K. Chen, X. Xu, R. Xia, L. Zhu, *Nanoscale* **2019**, 11, 7813.
- [60] Y. Pi, Z. Li, D. Xu, J. Liu, Y. Li, F. Zhang, G. Zhang, W. Peng, X. Fan, *ACS Sustainable Chem. Eng.* **2017**, 5, 5175.
- [61] B. Bera, A. Chakraborty, T. Kar, P. Leuaa, M. Neergat, *J. Phys. Chem. C* **2017**, 121, 20850.
- [62] S. Park, T. Schultz, X. Xu, B. Wegner, A. Aljarb, A. Han, L.-J. Li, V. C. Tung, P. Amsalem, N. Koch, *Commun. Phys.* **2019**, 2, 109.
- [63] J. Dendooven, C. Detavernier, *Atomic Layer Deposition in Energy Conversion Applications* (Ed: J. Bachmann), Wiley, Hoboken, NJ **2017**, Ch 1.